energies

MDPI

Article

Influence of Fluid Viscosity on Cavitation Characteristics of a Helico-Axial Multiphase Pump (HAMP)

Kaijie Ye [1], Denghui He [1,2,*], Lin Zhao [1] and Pengcheng Guo [1,2]

[1] Institute of Water Resources and Hydro-Electric Engineering, Xi'an University of Technology, No. 5 Jinhua South Road, Xi'an 710048, China
[2] State Key Laboratory of Eco-Hydraulic in Northwest Arid Region, Xi'an University of Technology, No. 5 Jinhua South Road, Xi'an 710048, China
* Correspondence: hedenghui@xaut.edu.cn

Abstract: Fluid viscosity is one of the key factors affecting the cavitation characteristics of the Helico-axial Multiphase Pump (HAMP). In this paper, fluids with viscosities of 24.46 mm^2/s, 48.48 mm^2/s, 60.70 mm^2/s, and 120.0 mm^2/s were investigated by numerical simulation. The Ansys Fluent software was employed to conduct the simulation. The mixture multiphase flow model and the RNG k-ε turbulence model were adopted. The Singhal cavitation model was employed to consider the effects of the non-condensable gas on cavitation. An experiment was carried out to validate the numerical method. The results showed that the Net Positive Suction Head-available (NPSHA) of the pump decreased as the fluid viscosity increased. Under the critical NPSHA condition, the NPSHA decreased from 5.11 m to 3.68 m as the fluid viscosity increased from 24.46 mm^2/s to 120.0 mm^2/s. This suggested that the cavitation performance of the pump was deteriorated under high fluid viscosity. The impeller passage area occupied by the vapor increased when the fluid viscosity increased. Nearly half of the flow passages were occupied by cavitation bubbles when the fluid viscosity increased to 120.0 mm^2/s. The vapor volume fraction, both on the suction surface and pressure surface of the blade, increased with the fluid viscosity. The vapor on the suction surface was mainly distributed in the region with the streamwise between 0 and 0.36 when the fluid viscosity was 24.46 mm^2/s; while the high vapor volume fraction range increased to the streamwise of 0.42 when the fluid viscosity increased to 120.0 mm^2/s. The higher vapor volume fraction corresponded with the lower pressure. It was also found that the turbulent kinetic energy, both on the suction surface and pressure surface, increased with the fluid viscosity, which was the favorite for producing more cavitation bubbles. Furthermore, the maximum velocity area was mainly concentrated in the inlet area of the impeller. The velocity distribution in the impeller was basically the same with the viscosity of 24.46 mm^2/s and 48.48 mm^2/s. When the viscosity further increased to 60.70 mm^2/s, the maximum velocity area in the impeller was relatively large. This study provides a reference for designing the HAMP.

Keywords: numerical simulation; Helico-axial multiphase pump; fluid viscosity; cavitation; Net Positive Suction Head

check for updates

Citation: Ye, K.; He, D.; Zhao, L.; Guo, P. Influence of Fluid Viscosity on Cavitation Characteristics of a Helico-Axial Multiphase Pump (HAMP). *Energies* **2022**, *15*, 8149. https://doi.org/10.3390/en15218149

Academic Editor: Enrico Nobile

Received: 23 September 2022
Accepted: 28 October 2022
Published: 1 November 2022

1. Introduction

The oil–gas multiphase pump is the key equipment in deep-sea oil and gas production and transportation. The Helico-axial Multiphase Pump (HAMP) shows great potential in offshore oil and gas exploitation and transportation because of its advantages, including compact structure, large flow rate, insensitivity to solid particles, and a wide gas application range [1,2]. The characteristics of the HAMP have been investigated by many researchers.

Visual experiments were conducted by Zhang et al. [3] to observe the two-phase flow pattern of the HAMP. It was found that when the gas volume fraction at the pump inlet increased, four flow patterns, i.e., the bubble flow, the agglomerated bubble flow, the gas pocket flow, and the separated flow, were observed. Serena et al. [4] also observed the similar flow pattern by using high-speed photography technology. Zhang et al. [5] used high-speed photography to investigate the characteristics of bubble movement and their distribution in a multiphase pump. Liu et al. [6] and Suh et al. [7] also explored the bubble trajectory in a pump by numerical simulation using ANSYS CFX software. The inhomogeneous Eulerian–Eulerian multiphase model and the shear stress transport (SST) k-ω turbulence model were employed. They concluded that the drag force, the lift force, the virtual mass force, and the turbulent diffusion force were also very important for accurately describing the unsteady two-phase transport process. Zhang et al. [8] investigated the effects of interphase forces on the flow in a HAMP. In their study, the non-uniform bubble model (NUBM) was adopted. They reported that interphase forces cannot be ignored under high inlet gas volume fractions. Hence, the non-uniform bubble model was recommended by them to better understand the flow characteristics in the HAMP. Zhang et al. [9] discussed the effects of blade tip clearances on pressure pulsation and tip leakage vortex. The results showed that pressure rises decreased for the single-phase liquid flow and the two-phase flow when the tip clearance size increased. In addition, the main frequency and amplitude of pressure pulsation in the pump also increased when the tip clearance increased.

The structure optimization of the HAMP is also one important aspect that researchers focused on. Zhang et al. [10] proposed several measures, such as using short blades, blade surface openings, and T-shaped blades to improve the gas–liquid phase mixing in a multiphase pump impeller under high gas void fraction. The RNG k-ε turbulence model and Euler two-phase model were selected with an inlet bubble diameter of 0.6 mm. They found that the gas–liquid two-phase mix degree was improved, and the gas–liquid separation was inhibited to some extent by using the appropriate measures. Tan et al. [11] also investigated the influence of the T-shaped blade end on the performance of the mixed transport pump. They found that the efficiency of the pump with the T-shaped blade end was improved, and the leakage flow was reduced compared with the original blade end. Xiao et al. [12] proposed a design method of controllable velocity moments for a multiphase pump. The numerical results by ANSYS CFX software suggested that the rotor–stator interaction and gas–liquid interaction could be suppressed by the best velocity moment distribution. Consequently, the pressure increment and efficiency of the pump were improved.

The cavitation characteristic of the pump is an important parameter to characterize the performance of the HAMP. Shi et al. [13] explored the cavitation phenomenon in the HAMP using numerical simulation. The standard k-ε turbulence model and the homogeneous multiphase flow model were used. The Zwart–Gerber–Belamari cavitation model based on the Rayleigh–Plesset equation was adopted. The results showed that cavitation affected the flow in the impeller. Under the serious cavitation condition, the vortex at the end of the cavitation area accelerated the instability and energy dissipation of the pump. Experimental investigations by Ge et al. [14–17] showed that the fluid temperature affected the hydrodynamic cavitation performance. The increase in the fluid temperature induced the growth of the cavitation volume up to about 55 °C; thereafter, an additional increase in temperature had the opposite effect. They also discussed the intensity and regime changing of hydrodynamic cavitation, considering temperature effects. Thus, the thermal effect could play a key role in investigating the cavitation characteristics of the pump. The fluid viscosity is another significant factor affecting the cavitation characteristics of a pump [18,19]. A number of researchers have reported on the influence of fluid viscosity on the pump performance. The field experimental results of Gié et al. [20] on a Poseidon multiphase pump showed that the efficiency and pressure increment capability of the HAMP decreased when transporting high viscosity fluid. Liu et al. [21] also reported that the head and efficiency of the HAMP gradually reduced with the rise in viscosity. They pointed out that most times, there was no large difference between numerical results using different turbulent models. Moreover, Patil et al. [22] and Ofuchi et al. [23] investigated the effect of fluid viscosity on centrifugal pumps. They noted that the pump head decreased when handling highly viscous flows.

At present, researchers have performed a lot of investigations on different flow conditions and parameters affecting the performance of the pump, such as the inlet gas volume fraction, the geometry, and the viscosity. However, little research has been devoted to the cavitation characteristics of the HAMP, in particular, the effects of fluid viscosity on the cavitation.

In this study, numerical simulation was performed to investigate the influence of the fluid viscosity on the cavitation characteristics of a HAMP. The simulation method was first established and validated by experiment. Then, the cavitation characteristic curve was obtained. The cavitation bubble distribution in the impeller and on the blade surface were also discussed. Finally, the effect of pressure and turbulent kinetic energy on the vapor volume fraction distribution, as well as the velocity distribution in the impeller, were analyzed.

2. Numerical Simulation Method

2.1. HAMP Geometry Model

The designed flow rate of the HAMP, Q_d, was 100 m^3/h, the designed water head, H_d, was 20 m, and the rotational speed, n, was 4500 rpm. The impeller and diffuser of the HAMP was modelled by the CFturbo software. The shroud diameter was 135 mm for both of the impeller and diffuser. The inlet and outlet diameter of the hub for the impeller were 94.5 mm and 105 mm, respectively, and those for the diffuser were 105 mm and 94.5 mm, respectively. The axial length of the impeller and diffuser was equal, which was 50 mm. The blade numbers of the impeller and diffuser were 4 and 15, respectively. The big blade wrap angle was employed by the impeller, which was 175.5°, and a small blade wrap angle with 25.6° was used by the diffuser. The 0.4% of the shroud diameter was adopted as the tip clearance value, which was 0.54 mm. There was no tip clearance for the diffuser. The main parameters of the HAMP are shown in Table 1.

Table 1. Main parameters of HAMP.

Parameter	Impeller	Diffuser	Unit
Shroud diameter	135	135	mm
Hub inlet diameter	94.5	105	mm
Hub outlet diameter	105	94.5	mm
Axial length	50	50	mm
Number of blades	4	15	-
Blade wrap angle	175.5	25.6	°
Tip clearance	0.54	0	mm

The three-dimensional structure of the calculation domain is shown in Figure 1. For the convenience of calculation, the lengths of the inlet and outlet sections were extended to 2 and 6 times the axial length of the impeller, respectively. This ensured that the flow in the inlet and outlet pipes was fully developed.

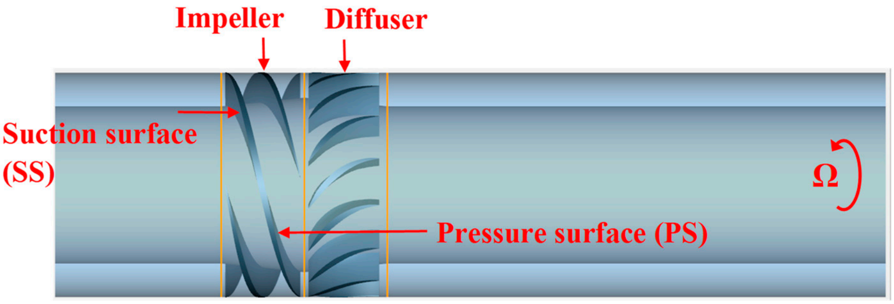

Figure 1. Three-dimensional model of HAMP (Ω denotes rotational direction).

2.2. Meshing of Calculation Domain

The cavitation in the impeller was investigated in the present study. The calculation domain was divided into three components, i.e., the inlet section, the impeller, and the outlet section. The polyhedral mesh divided by Fluent Meshing software was employed. The meshes around the blades were densified (Figure 2). Four groups of meshes were selected for mesh independence verification. The mesh number of each component is shown in Table 2. According to Figure 3, it was found that the water head and efficiency of the HAMP reduced by 0.68% and 0.84%, respectively, when the mesh number increased from group 3 to group 4. Considering the calculation resources and accuracy, the group 3 mesh was finally used for simulation. The total mesh number (*N*) was 5,703,986.

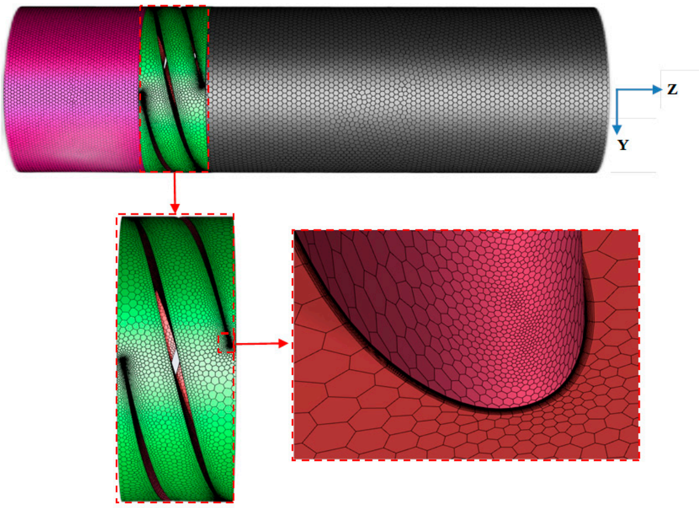

Figure 2. Meshes of HAMP.

Table 2. Mesh cells of different parts.

Component	Mesh Number (*N*)			
	1	**2**	**3**	**4**
Inlet section	63,290	175,915	197,788	255,099
Impeller	1,758,452	3,668,160	5,275,676	6,570,704
Outlet section	178,913	186,142	230,522	292,592
Total mesh number	2,000,655	4,030,217	5,703,986	7,118,395

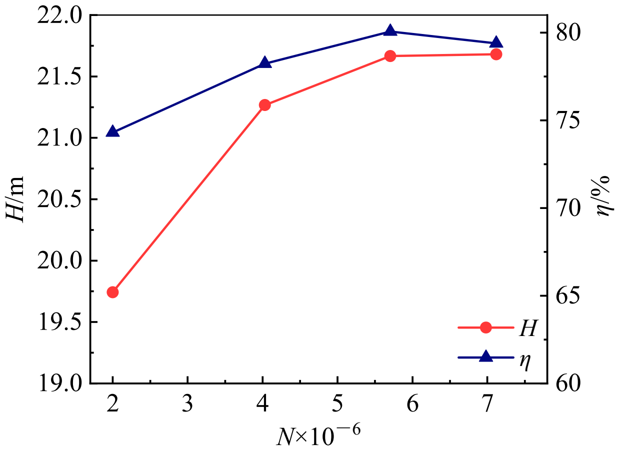

Figure 3. Mesh independence analysis.

2.3. Numerical Scheme

The fluids used in the present simulation were machine oils that have been employed by Li [14] and Li and Zhang [24]. Their density, kinematic viscosity, saturated vapor pressure, and surface tension are shown in Table 3. Studies by Nakamura et al. [25] and Washio et al. [26] showed that the temperature and viscosity exhibited a neglected effect on the surface tension and saturated vapor pressure for those machine oils. Consequently, the surface tension and saturated vapor pressure of the viscous oils were considered to be constant, i.e., 3.0×10^{-2} N/m and 4000 Pa. In addition, Ishihara [27] reported that the concentration of non-condensable gas in the viscous oil was above 40 ppm. Thus, the effect of the non-condensable gas on cavitation was also taken into account. The non-condensable gas content was 40 ppm in the present simulation.

Table 3. Properties of four liquids and their vapors at 20 °C [14,24].

Fluid No.	Medium	Density (kg/m^3)	Kinematic Viscosity (mm^2/s)	Dynamic Viscosity (Pa·s)	Saturated Vapor Pressure (Pa)	Surface Tension (N/m)	Non-Condensable Gas Content (ppm)
1	Liqud	839	24.46	2.0530×10^{-2}	4000.0	3.0×10^{-2}	40
	Vapor	0.4650	0.5916	2.7511×10^{-4}			
2	Liqud	851	48.48	4.1256×10^{-2}	4000.0	3.0×10^{-2}	40
	Vapor	0.4716	1.1723	5.5284×10^{-4}			
3	Liqud	858	60.70	5.2081×10^{-2}	4000.0	3.0×10^{-2}	40
	Vapor	0.4755	1.4881	7.0760×10^{-4}			
4	Liqud	865	120.0	1.0380×10^{-1}	4000.0	3.0×10^{-2}	40
	Vapor	0.4796	2.1364	1.0246×10^{-3}			

The numerical simulation scheme is shown in Table 4. The Mixture model was used as the multiphase flow model. The Singhal model was employed and the effect of the non-condensable gas on the cavitation was considered [28]. The RNG k-ε turbulence model was adopted, which has been proven to characterize the flow in HAMP well [10,13]. The inlet and outlet boundaries were the pressure inlet and mass flow outlet, respectively. The calculation results of the single-phase oil without cavitation were employed as the initial value of cavitation calculation. Then, the pump inlet absolute pressure was gradually reduced to investigate the cavitation characteristics in the pump.

Table 4. Numerical simulation scheme.

Project	Parameter
Multiphase flow model	Mixture model
Cavitation Model	Singhal model
Turbulence model	RNG k-ε
Inlet boundary	Pressure inlet
Outlet boundary	Mass flow outlet
Wall condition	Smooth, no-slip wall
Pressure-velocity coupling	Coupled
Moment spatial discretization	Second Order Upwind

2.4. Cavitation Model

The non-condensable gas contained in the oil affects the cavitation performance of the pump, so its influence should be considered. The governing equations of the Singhal cavitation model are given by Singhal et al. [29]:

$$\nabla \cdot \left(f_v \rho \vec{v}_v \right) = \nabla \cdot (\Gamma \nabla f_v) + \dot{m}^+ - \dot{m}^- \tag{1}$$

where f_v is the vapor mass fraction, ρ is the mixture density, and $\dot{m}^+$ and $\dot{m}^-$ are the evaporation rate and condensation rate, respectively, which are given by Equations (2) and (3):

$$\dot{m}^+ = F_{vap}\frac{\max\left(1.0, \sqrt{k}\right)\left(1 - f_v - f_g\right)\rho_v\rho_l}{\sigma}\sqrt{\frac{2}{3}\frac{p_v - p}{\rho_l}} \quad , p \le p_v \tag{2}$$

$$\dot{m}^- = F_{cond}\frac{\max(1.0, \sqrt{k}) f_v\rho_v\rho_l}{\sigma}\sqrt{\frac{2}{3}\frac{p - p_v}{\rho_l}} \quad , p > p_v \tag{3}$$

where f_g is the mass fraction of non-condensable gas, k is turbulent kinetic energy, ρ_v and ρ_l are vapor and liquid density, respectively, σ is the surface tension coefficient, F_{vap} is the evaporation coefficient ($F_{vap} = 0.02$), F_{cond} is the condensation coefficient ($F_{cond} = 0.01$), and ρ_v is the saturation vapor pressure considering the influence of turbulent pressure fluctuation:

$$p_v = p_{sat} + \frac{1}{2}(0.39\rho k) \tag{4}$$

where p_{sat} is the saturation vapor pressure of the fluid at the current temperature.

2.5. Numerical Method Validation

The numerical method was validated by experiment. The pump experimental system is shown in Figure 4. The water was pumped from the water tank by the multistage centrifugal pump and then measured by the mass flowmeter (the uncertainty was ±0.1%). After flowing through a straight pipe section, the water entered the HAMP. Finally, the water returned to the water tank for recycling. The inlet pressure of the pump was measured by a Rosemount 3051CG pressure sensor (the uncertainty was ±0.075%), and the differential pressure between the inlet and outlet of the pump was measured by a Rosemount 3051CD differential pressure sensors (the uncertainty was ±0.075%). The liquid flow rate, the pressure, the differential pressure, and other signals were collected by a data acquisition device; then, they were displayed and stored in a computer. Tap water was employed in the experiment.

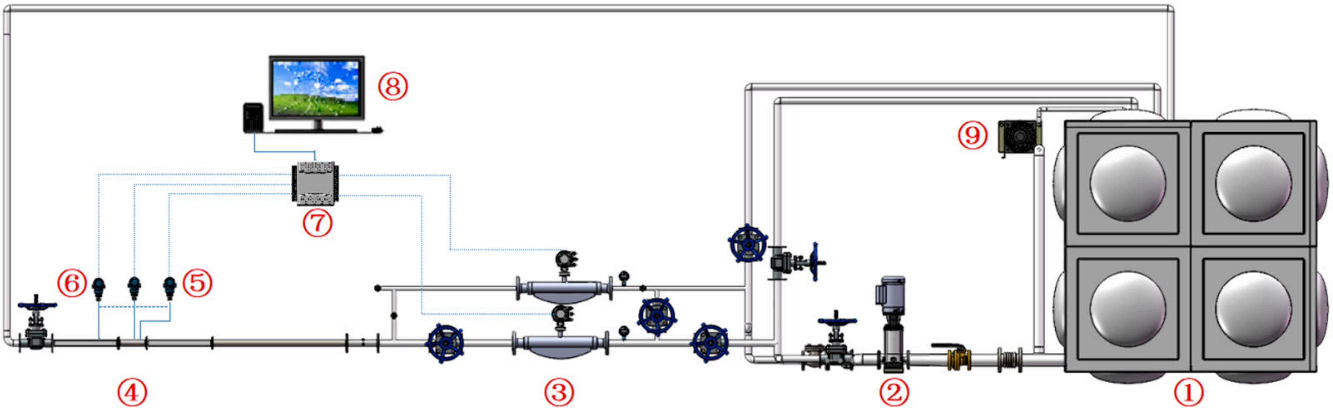

Figure 4. Flow chart of experimental system: ① water tank, ② centrifugal pump, ③ Coriolis mass flowmeter, ④ HAMP test section, ⑤ pressure sensor, ⑥ differential pressure sensor, ⑦ data acquisition device, ⑧ computer, ⑨ heat exchanger.

The water head between the simulation and experimental results was compared. As shown in Figure 5, the maximum relative error of the water head was within ±5.0%, which suggested that the present method was reliable and accurate.

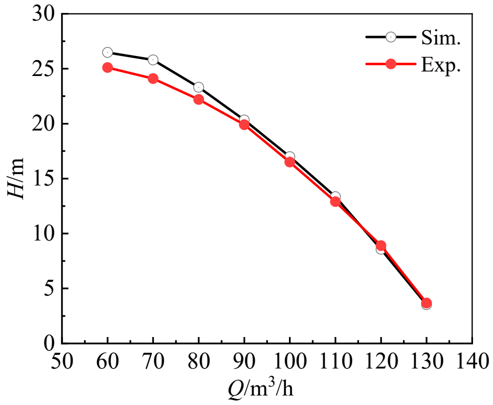

Figure 5. Water head comparison between simulation and experiment.

3. Results and Discussions

3.1. Cavitation Characteristic Curve of HAMP

The Net Positive Suction Head-available (NPSHA) is calculated by Equation (5):

$$\text{NPSHA} = \frac{p_{in} - p_{sat}}{\rho_l g} + \frac{v_{in}^2}{2g} \tag{5}$$

where p_{in} is the absolute pressure of the pump inlet, p_{sat} is the saturation vapor pressure under the temperature of 20 °C, v_{in} is the average velocity in the pump inlet, and g is the gravitational acceleration.

The head degradation rate is denoted by Δ and is defined by Equation (6):

$$\Delta = \frac{\delta H}{H_{noncav}} \times 100\% = \left(\frac{H_{noncav} - H_{cav}}{H_{noncav}} \right) \times 100\% \tag{6}$$

where H_{cav} and H_{noncav} are the head with cavitation occurrence and without cavitation occurrence in the pump, respectively.

In the present study, the head degradation rate, Δ, was 3%, and was defined as the critical Net Positive Suction Head-available (NPSHA$_C$) [30].

Figure 6 shows the pump water head variation with the NPSHA under different fluid viscosities. It can be seen that the head of the HAMP decreased gradually with the reduction in the NPSHA. When the NPSHA reduced to a certain value, the head dropped sharply, which indicated that the "fracture" condition occurred [13]. Under the same NPSHA, the HAMP head decreased as the fluid viscosity increased.

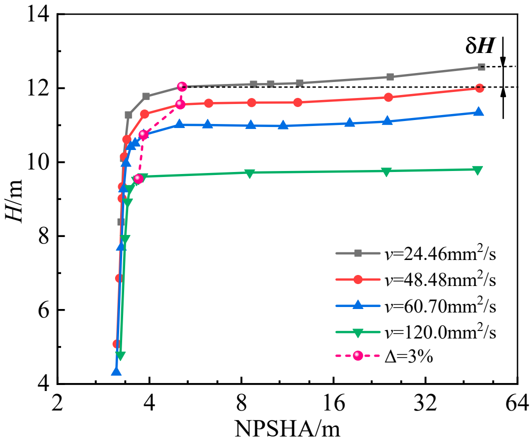

Figure 6. Cavitation characteristic curve of the HAMP under different fluid viscosities (Q_d = 100 m^3/h, n = 4500 rpm).

Under the NPSHA$_C$ condition, the NPSHA under different fluid viscosities is shown in Figure 7. We found that the NPSHA decreased with the increasing fluid viscosity. It decreased from 5.11 m to 3.68 m as the fluid viscosity increased from 24.46 mm^2/s to 120.0 mm^2/s. This suggested that the cavitation performance of the HAMP was deteriorated under the critical cavitation condition by increasing the fluid viscosity. The cavitation was more prone to appear in the pump impeller under high viscosity conditions. Li and Zhang [24] also found that an increased viscosity was favorable to cavitation in a pump as the turbine.

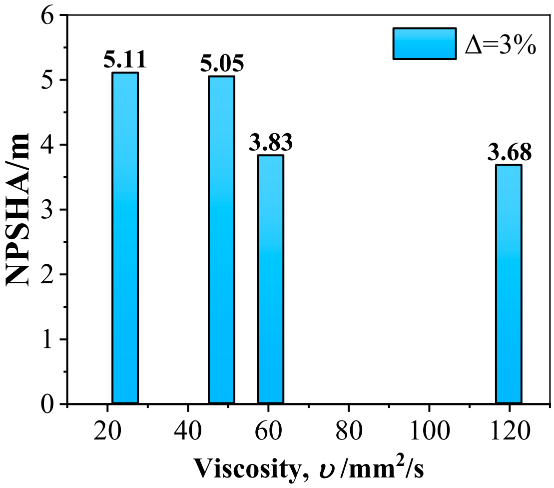

Figure 7. NPSHA under different fluid viscosity (Q_d = 100 m^3/h, n = 4500 rpm).

The cavitation number, σ_a, is one of the important parameters characterizing the cavitation of the pump. It is defined by Equation (7):

$$\sigma_{\text{a}} = \frac{p_{in} - p_{sat}}{\frac{1}{2}\rho_l U^2} \tag{7}$$

$$U = \frac{n\pi D}{60} \tag{8}$$

where U is the circumferential velocity at the intersection of the inlet edge of the impeller blade and the hub, and D is the impeller diameter.

The Reynolds number is given by Equation (9):

$$Re = \frac{UD}{v} \tag{9}$$

The relationship between the σ_a and Re under the head degradation rate of 3% is shown in Figure 8. It was found that the cavitation number increased from 0.08213 to 0.08574 when the Re increased from 3.58×10^4 to 8.73×10^4, which indicated that the pump more easily cavitated under a lower Re. When the Re further increased to 1.73×10^5, the σ_a was almost unchanged. Therefore, the pump cavitation characteristics would be deteriorated as the fluid viscosity increased when the flow rate was held constant. Studies by Pelz et al. [31] also demonstrated that the Reynolds number was correlated with the cavitation number, and different cavitation regimes existed in different flow conditions. More data are required to develop a correction model for predicting the cavitation number of the HAMP when transporting viscosity fluids other than pure water.

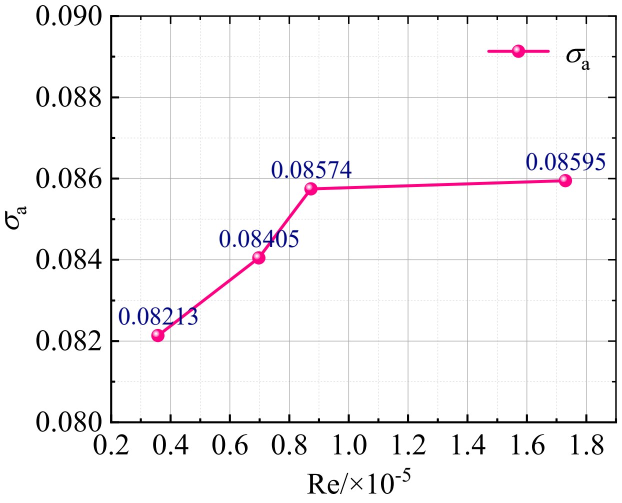

Figure 8. Relationship between cavitation number σ_a and Re under head degradation rate of 3% (Q_d = 100 m^3/h, n = 4500 rpm).

3.2. VVF Distribution in Impeller Passage

As shown in Figure 9, the cavitation vapor phase was mainly distributed on the suction surface of the blade. The vapor volume fraction (VVF) reduced along the flow in the impeller passage. Under the critical cavitation condition (Δ = 3%), the VVF was basically unchanged as the fluid viscosity increased from 24.46 mm^2/s to 48.48 mm^2/s. Then, the VVF around the LE significantly declined as the fluid viscosity increased to 60.70 mm^2/s. If the fluid viscosity was further increased, the VVF was almost unaffected by it. This agreed well with the NPSHA shown in Figure 7. We also found that the vapor phase occupied more area of the impeller passage as the fluid viscosity increased. Nearly half of the flow passages were occupied by cavitation bubbles when the fluid viscosity increased to 120.0 mm^2/s.

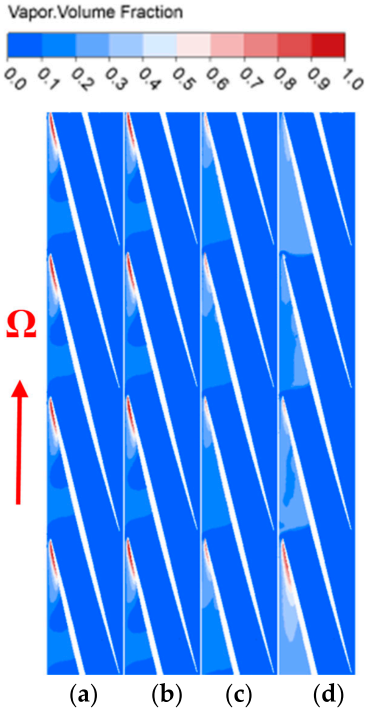

Figure 9. VVF distribution at 0.5 times blade height in impeller passage under critical cavitation condition (Δ = 3%): (**a**) ν = 24.46 mm^2/s; (**b**) ν = 48.48 mm^2/s; (**c**) ν = 60.70 mm^2/s; (**d**) ν = 120.0 mm^2/s.

3.3. VVF on Blade Surface

To further quantitatively analyze the cavitation in the impeller, the VVF on the suction surface (SS) and pressure surface (PS) along the blade streamline at 0.5 times the blade height is shown here in Figure 10.

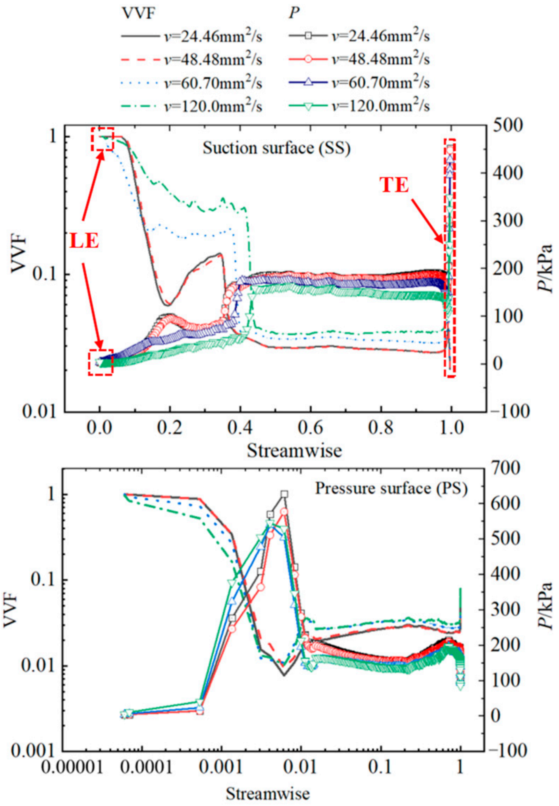

Figure 10. VVF and pressure distribution on suction surface (SS) and pressure surface (PS) along the blade streamline at 0.5 times blade height ($\Delta = 3\%$).

The abscissa represents a dimensionless length of a blade from the leading edge (LE) to the trailing edge (TE). 0 and 1 are the positions of LE and the TE, respectively. It can be seen that the maximum VVF appeared at the LE of the blade and the value could reach 1. The VVF on the SS was generally larger than that on the PS. The VVF on the PS was almost unchanged along the streamwise, except at the LE and TE of the blade. It was also found that the pressure distribution exhibited the opposite trend with the VVF distribution, where the high VVF corresponded to low pressure.

With the increase in the fluid viscosity, the VVF on the SS was gradually spread out from the LE to the TE of the blade, and the VVF on both the SS and PS increased with the fluid viscosity. For example, when the fluid viscosity was 24.46 mm^2/s, the vapor on the SS was mainly distributed in the region with the streamwise between 0 and 0.36; while the high VVF range increased to the streamwise of 0.42 when the fluid viscosity increased to 120.0 mm^2/s. And the VVF in this region also approximately increased from 0.1 to 0.3.

According to Equation (4), the saturation vapor pressure, p_v is affected by the turbulent kinetic energy, k. The p_v increased as the k increased, which indicated that the liquid evaporated more easily (Equation (3)) and was harder to condensate (Equation (4)). Figure 11 shows the turbulent kinetic energy on the blade suction surface (SS) and pressure surface (PS) of the blades. It can be observed that k declined from the LE to the TE along the blade. Hence, the cavitation was more serious around the LE. In addition, the k on both the SS and PS increased with the fluid viscosity. Thus, more cavitation bubbles were produced as the fluid viscosity increased.

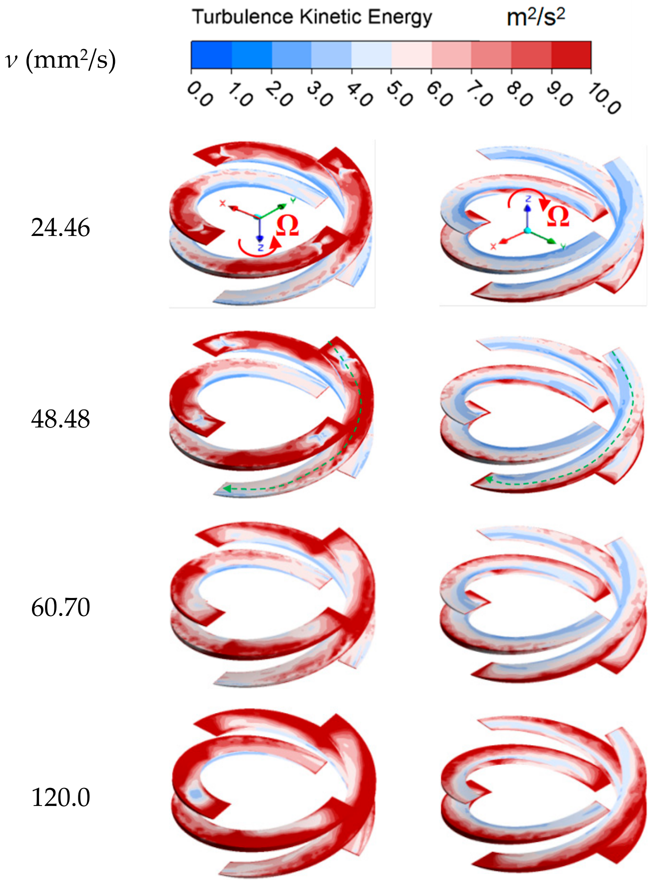

(**a**) (**b**)

Figure 11. Distribution of turbulent kinetic energy on blade: (**a**) suction surface (SS) and (**b**) pressure surface (PS) (Δ = 3%, the green dash lines represents the streamline at 0.5 times blade height).

3.4. Velocity Distribution in Impeller

The velocity contours at 0.5 times blade height in the impeller passage under the critical cavitation condition are shown in Figure 12. It can be seen that the maximum velocity area was mainly concentrated in the inlet area of the impeller. The velocity distribution in the impeller was basically the same with the viscosity of 24.46 mm^2/s and 48.48 mm^2/s. When the viscosity was further increased to 60.70 mm^2/s, the maximum velocity area in the impeller was relatively large. This may be attributed to more area of the impeller passage being occupied by the cavitation bubbles as the viscosity increased (see Figure 9). Thus, the velocity of the mixture increased, when compared with the conditions with less cavitation bubbles.

Figure 13 displays the velocity profile in the impeller of the HAMP with different liquid viscosities under the critical cavitation condition (Δ = 3%). We found that the velocity in the front of the impeller (axial length was between 0 and 5 mm) fluctuated significantly, and dropped rapidly to zero near the blade, and then recovered quickly. The velocity variation under different viscosities showed a similar tendency. The liquid viscosity affected the velocity; in particular, when the viscosity increased to 120.0 mm^2/s, the maximum velocity in the axial length of the impeller between 5 mm and 15 mm was obviously greater than that of under other viscosities. In addition, the velocity profile in Figure 13 was in good agreement with the velocity contours in Figure 12.

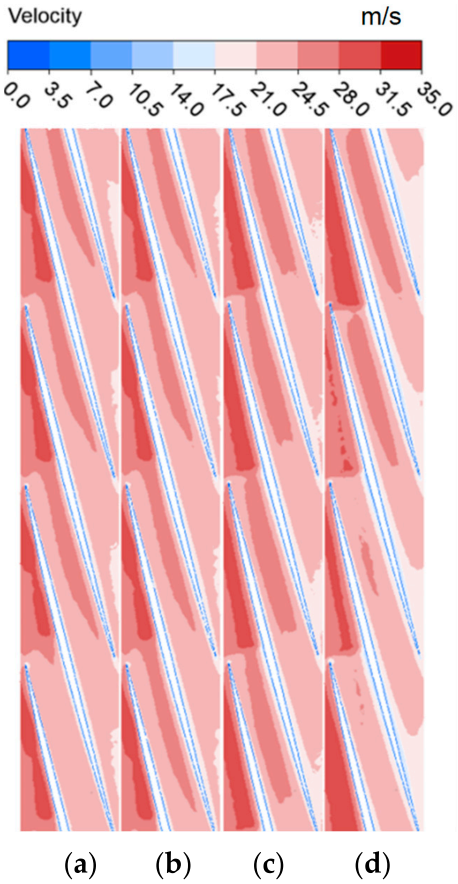

Figure 12. Velocity contours at 0.5 times blade height in impeller passage under critical cavitation condition (Δ = 3%): (**a**) ν = 24.46 mm^2/s; (**b**) ν = 48.48 mm^2/s; (**c**) ν = 60.70 mm^2/s; (**d**) ν = 120.0 mm^2/s.

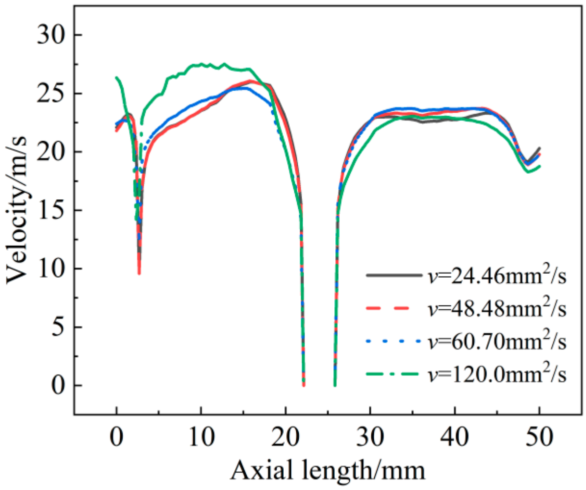

Figure 13. Velocity profile in the impeller of the HAMP with different liquid viscosities under critical cavitation condition (Δ = 3%).

4. Conclusions

The influence of fluid viscosity on cavitation characteristics of a Helico-axial Multiphase Pump (HAMP) was investigated by numerical simulation. The cavitation characteristic curve of the pump was discussed. The influence mechanism of fluid viscosity on the cavitation of the HAMP was revealed by analyzing the effect of the pressure and turbulent kinetic energy on vapor volume fraction (VVF) distribution. The velocity distribution in the impeller was also analyzed. The following conclusions may be drawn:

(1) The Net Positive Suction Head-available decreased as the fluid viscosity increased under the critical cavitation condition. It decreased from 5.11 m to 3.68 m as the fluid viscosity increased from 24.46 mm^2/s to 120.0 mm^2/s. Cavitation was more prone to occur in the pump impeller under high viscosity condition. The cavitation number increased from 0.08213 to 0.08574 when the Reynolds number increased from 3.58×10^4 to 8.73×10^4, which also demonstrated that the pump cavitation characteristics would be deteriorated as the fluid viscosity increased when the flow rate was held constant.

(2) In general, the VVF reduced along the impeller passage. Under the critical cavitation condition, the VVF was basically unchanged as the fluid viscosity increased from 24.46 mm^2/s to 48.48 mm^2/s. Then, the VVF around the leading edge of the blade significantly reduced as the fluid viscosity increased to 60.70 mm^2/s. The area occupied by the vapor increased with the fluid viscosity. Nearly half of the flow passages were occupied by cavitation bubbles when the fluid viscosity increased to 120.0 mm^2/s.

(3) The VVF on the suction surface was gradually spread out from the leading edge to the trailing edge of the blade, and the VVF on both the suction surface and pressure surface increased with the fluid viscosity. When the fluid viscosity was 24.46 mm^2/s, the vapor on the suction surface was mainly distributed in the region with the streamwise between 0 and 0.36; while the high VVF range increased to the streamwise of 0.42 when the fluid viscosity increased to 120.0 mm^2/s. The VVF in this region also approximately increased from 0.1 to 0.3.

(4) The pressure distribution exhibited the opposite trend with the VVF distribution. The decrease in the pressure in the impeller led to the increase in the cavitation bubble. The turbulent kinetic energy on both the suction surface and pressure surface increased with the fluid viscosity, which also resulted in more cavitation bubbles being produced. The velocity distribution in the impeller suggested that the velocity was basically the same with the viscosity of 24.46 mm^2/s and 48.48 mm^2/s. When the viscosity was further increased to 60.70 mm^2/s, the maximum velocity area in the impeller was relatively large.

In conclusion, the cavitation characteristics of the HAMP were significantly affected by the fluid viscosity. More data are required for developing a model to consider the fluid viscosity when designing the HAMP.

Author Contributions: Conceptualization, K.Y. and D.H.; methodology, K.Y. and L.Z.; software, L.Z.; validation, K.Y. and D.H.; investigation, K.Y. and L.Z.; writing—original draft preparation, K.Y. and D.H.; writing—review and editing, K.Y., D.H. and P.G.; supervision, D.H. and P.G.; project administration, D.H.; funding acquisition, D.H. and P.G. All authors have read and agreed to the published version of the manuscript.

Funding: This research was funded by the Scientific Research Program for Youth Innovation Team Construction of the Shaanxi Provincial Department of Education, grant number 21JP087 and the National Natural Science Foundation of China, grant number 51839010 and 51709227.

Data Availability Statement: The data can be shared up on request.

Conflicts of Interest: The authors declare no conflict of interest.

References

1. Gong, H.; Gioia, F.; Catalin, T.; Morrison, G. Comparison of multiphase pumping technologies for subsea and downhole applications. *SPE Annu. Tech. Conf. Exhib.* **2011**, *1*, 36–46.
2. Zhu, J.; Zhang, H.Q. A review of experiments and modeling of gas-liquid flow in electrical submersible pumps. *Energies* **2018**, *11*, 180. [CrossRef]
3. Zhang, J.; Cai, S.; Li, Y.; Zhu, H.; Zhang, Y. Visualization study of gas–liquid two-phase flow patterns inside a three-stage rotodynamic multiphase pump. *Exp. Therm. Fluid Sci.* **2016**, *70*, 125–138. [CrossRef]

4. Serena, A.; Bakken, L.E. Experimental study of the influence of the operating parameters on the performance and capability of a mixed-flow multiphase pump. In Proceedings of the ASME Turbo Expo 2016: Turbomachinery Technical Conference and Exposition, Seoul, Korea, 13–17 June 2016.
5. Zhang, W.; Zhu, B.; Yu, Z. Characteristics of bubble motion and distribution in a multiphase rotodynamic pump. *J. Petrol. Sci. Eng.* **2020**, *193*, 107435. [CrossRef]
6. Liu, M.; Cao, S.; Cao, S. Numerical analysis for interphase forces of gas-liquid flow in a multiphase pump. *Eng. Comput.* **2018**, *35*, 2386–2402. [CrossRef]
7. Suh, J.W.; Kim, J.W.; Choi, Y.S.; Kim, J.H.; Joo, W.G.; Lee, K.Y. Development of numerical Eulerian-Eulerian models for simulating multiphase pumps. *J. Petrol. Sci. Eng.* **2018**, *162*, 588–601. [CrossRef]
8. Zhang, W.; Yu, Z.; Li, Y. Application of a non-uniform bubble model in a multiphase rotodynamic pump. *J. Petrol. Sci. Eng.* **2019**, *173*, 1316–1322. [CrossRef]
9. Zhang, J.; Fan, H.; Zhang, W.; Xie, Z. Energy performance and flow characteristics of a multiphase pump with different tip clearance sizes. *Adv. Mech. Eng.* **2019**, *11*, 1687814018823356. [CrossRef]
10. Zhang, J.Y.; Zhu, H.W.; Ding, K.; Qiang, R. Study on measures to improve gas-liquid phase mixing in a multiphase pump impeller under high gas void fraction. *IOP Conf. Ser. Earth Environ. Sci.* **2012**, *15*, 062023. [CrossRef]
11. Tan, L.; Xie, Z.F.; Liu, Y.B.; Yue, H.; Yun, X. Influence of T-shape tip clearance on performance of a mixed-flow pump. *Proc. Inst. Mech. Eng. Part A J. Power Energy* **2018**, *232*, 386–396.
12. Xiao, W.; Tan, L. Design method of controllable velocity moment and optimization of pressure fluctuation suppression for a multiphase pump. *Ocean Eng.* **2020**, *220*, 108402. [CrossRef]
13. Shi, G.; Wang, S.; Xiao, Y.; Liu, Z.; Li, H.; Liu, X. Effect of cavitation on energy conversion characteristics of a multiphase pump. *Renew. Energ.* **2021**, *177*, 1308–1320. [CrossRef]
14. Li, W.G. Modeling viscous oil cavitating flow in a centrifugal pump. *J. Fluids Eng.* **2016**, *138*, 4031061. [CrossRef]
15. Ge, M.; Petkovšek, M.; Zhang, G.; Jacobs, D.; Coutier-Delgosha, O. Cavitation dynamics and thermodynamic effects at elevated temperatures in a small Venturi channel. *Int. J. Heat Mass Tran.* **2021**, *170*, 120970. [CrossRef]
16. Ge, M.; Manikkam, P.; Ghossein, J.; Subramanian, R.K.; Coutier-Delgosha, O.; Zhang, G. Dynamic mode decomposition to classify cavitating flow regimes induced by thermodynamic effects. *Energy* **2022**, *254*, 124426. [CrossRef]
17. Ge, M.; Zhang, G.; Petkovšek, M.; Long, K.; Coutier-Delgosha, O. Intensity and regimes changing of hydrodynamic cavitation considering temperature effects. *J. Clean. Prod.* **2022**, *338*, 130470. [CrossRef]
18. Ge, M.; Sun, C.; Zhang, G.; Coutier-Delgosha, O.; Fan, D. Combined suppression effects on hydrodynamic cavitation performance in Venturi-type reactor for process intensification. *Ultrason. Sonochem.* **2022**, *86*, 106035. [CrossRef]
19. Liu, M.; Tan, L.; Cao, S.L. Influence of viscosity on energy performance and flow field of a multiphase pump. *Renew. Energ.* **2020**, *162*, 1151–1160. [CrossRef]
20. Gié, P.; Buvat, P.; Bratu, C.; Durando, P. *Poseidon Multiphase Pump: Field Tests Results*; OnePetro: Houston, TX, USA, 1992.
21. Liu, P.; Wang, Y.; Yan, F.; Nie, C.; Ouyang, X.; Xu, J.; Gong, J. Effects of Fluid Viscosity and Two-Phase Flow on Performance of ESP. *Energies* **2020**, *13*, 5486. [CrossRef]
22. Patil, A.; Morrison, G. Affinity law modified to predict the pump head performance for different viscosities using the Morrison number. *J. Fluids Eng.* **2019**, *141*, 021203. [CrossRef]
23. Ofuchi, E.M.; Cubas, J.M.C.; Stel, H.; Dunaiski, R.; Vieira, T.S.; Morales, R.E.M. A new model to predict the head degradation of centrifugal pumps handling highly viscous flows. *J. Petrol. Sci. Eng.* **2020**, *187*, 106737. [CrossRef]
24. Li, W.G.; Zhang, Y.L. Computational cavitating viscous liquid flows in a pump as turbine and Reynolds number effects. *Proc. Inst. Mech. Eng. Part E J. Process Mech. Eng.* **2019**, *233*, 536–550. [CrossRef]
25. Nakamura, K.; Someya, T. Investigation into the tensile strength of real liquids: The application to lubricant oil. *Trans. JSME Ser. B* **1980**, *46*, 910–918. [CrossRef]
26. Washio, S.; Takahashi, S.; Uda, Y.; Sunahara, T. Study on cavitation inception in hydraulic oil flow through a long two-dimensional constriction. *Proc. Inst. Mech. Eng. Part J* **2002**, *215*, 373–386. [CrossRef]
27. Ishihara, T. Cavitation in Hydraulic Oil. *Trans. JSME Ser. B* **1982**, *48*, 1829–1832. [CrossRef]
28. ANSYS. *ANSYS, Release 19.0 ANSYS Documentation*; ANSYS Inc.: Washington County, PA, USA, 2019.
29. Singhal, A.K.; Athavale, M.M.; Li, H.; Jiang, Y. Mathematical basis and validation of the full cavitation model. *J. Fluids Eng.* **2002**, *124*, 617–624. [CrossRef]
30. Gülich, J.F. *Centrifugal Pumps*, 4th ed.; Springer: Berlin/Heidelberg, Germany, 2019; pp. 316–320.
31. Pelz, P.F.; Keil, T.; Gro, T.F. The transition from sheet to cloud cavitation. *J. Fluid Mech.* **2017**, *817*, 439–454. [CrossRef]